Supplement to: Constraining 2020 methane emissions in the EMME region using TROPOMI satellite data in an atmospheric inversion

Martin Vojta[1,2], Rakesh Subramanianl[1], Nikos Gialesakis[2,3], Rona L. Thompson[4], Andreas Stohl[1], and Maria Kanakidou[2]

[1]Department of Meteorology and Geophysics, University of Vienna, Vienna, Austria
[2]Department of Chemistry, Environmental Chemical Processes Laboratory (ECPL), University of Crete, Crete, Greece
[3]Institute of Environmental Physics, Laboratory for Modeling and Observation of the Earth System (LAMOS), and Center for Marine Environmental Sciences (MARUM), University of Bremen, Bremen, Germany
[4]NILU, Kjeller, Norway

Correspondence: Martin Vojta (martin.vojta@univie.ac.at)

S1 Super observations

In this section we compare two different methods for accumulating retrievals into super observations: (a) Thompson et al. (2025) assigned retrievals to the super-observation grid based on their midpoint coordinate, while we (b) subdivide each retrieval pixel into 25 sub-elements of equal area and assign each sub-element individually to the super observation grid, as illustrated in Fig. S1. In the midpoint-based method, each ground pixel is fully assigned to one super observation grid cell, neglecting partial contributions arising from pixels that extend across neighboring cells (see Fig. S1a). In the sub-element–based method, individual sub-elements may still partially overlap neighboring grid cells; however, their individual contributions are much smaller, and the resulting overlap error decreases as the number of sub-elements increases (see Fig. S1b). A total of 25 sub-elements was selected, as increasing this number further resulted in negligible changes. Figure S2 illustrates the differences between the two methods for the example day 02 October 2020, which features relatively good coverage over the investigated domain and is representative of the general difference between both approaches. Both methods produce very similar spatial patterns of super-observation mole fractions (Fig. S2a,b), which are difficult to distinguish without examining difference fields. Therefore, Fig. S2c and Fig. S2d present the absolute and relative differences, respectively. For most super-observation grid cells, differences remain very low (below 0.1%) and reach a few ppb in isolated cells only.

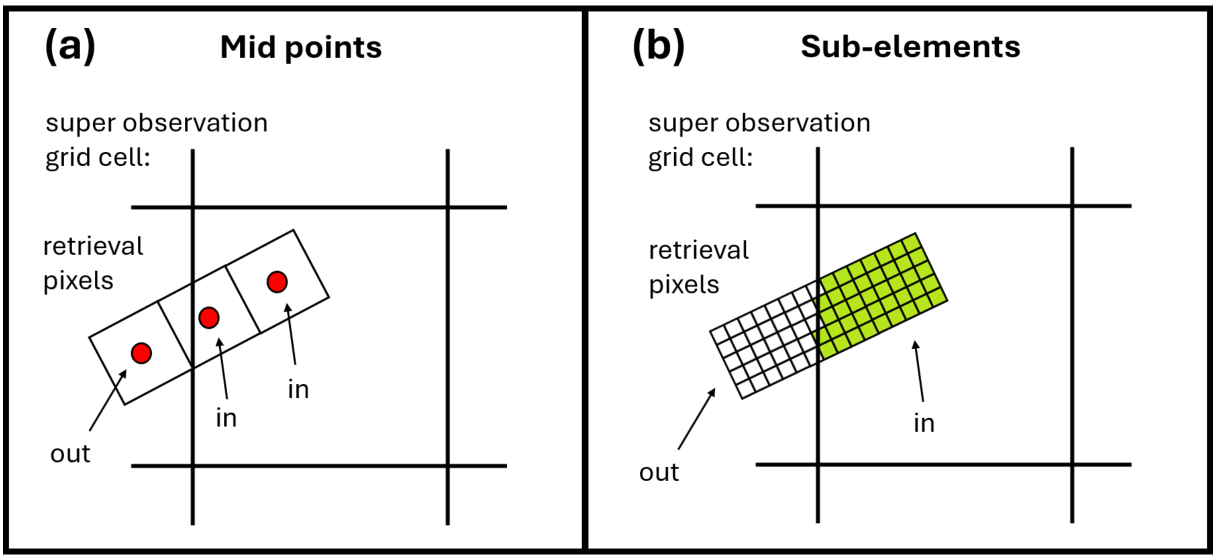

Figure S1. Illustration of the methods used to aggregate retrievals into super-observations: (a) retrievals are assigned to the super-observation grid based on their ground pixel midpoint coordinates; (b) retrieval pixels are subdivided into 25 equal-area elements, which are individually mapped onto the super-observation grid.

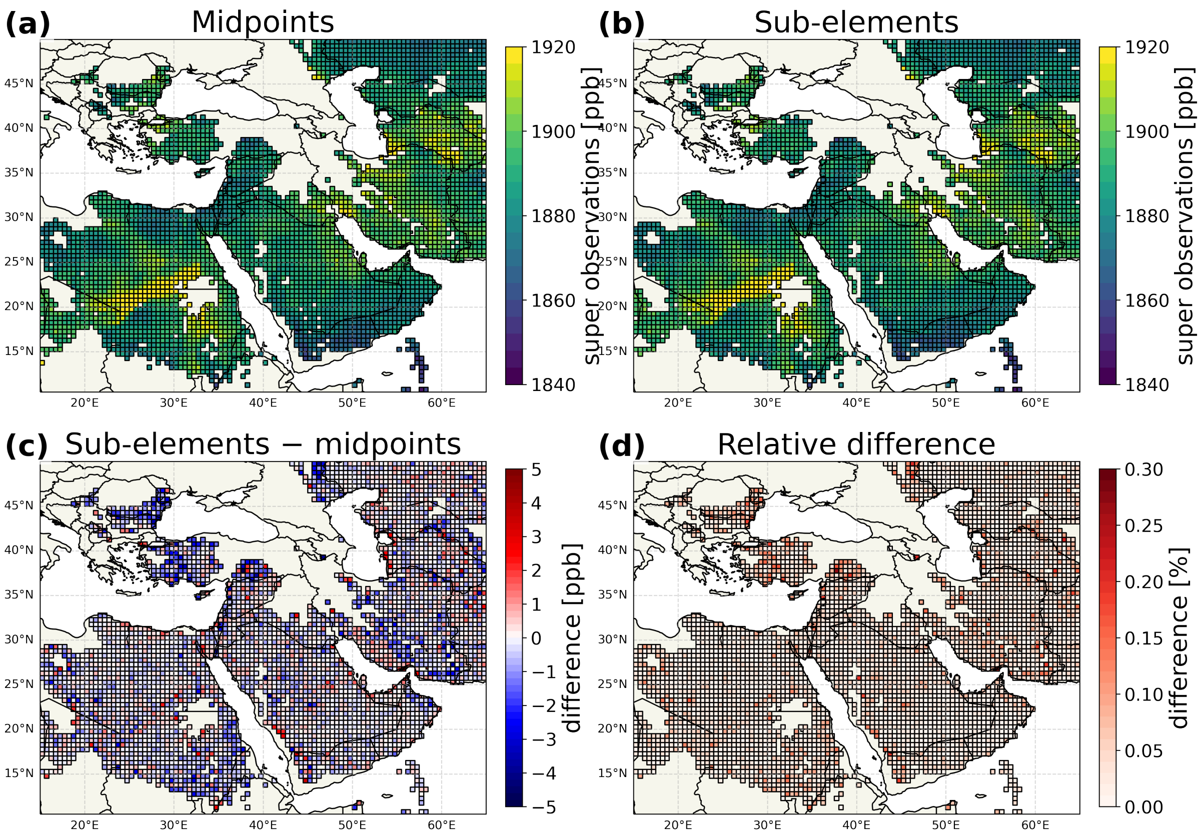

Figure S2. (a) Super observation column mole fractions derived using the midpoint-based method; (b) super-observation column mole fractions derived using the sub-element-based approach; (c) their absolute differences; and (d) their relative differences

S2 A priori emissions

Figure S3 illustrates the contributions of different sectors to the a priori emissions, as listed in Table S1. Figure S4 shows the subdivision of the fossil fuel exploitation sector into emissions from gas, oil, and coal, based on the recent GFEI v3 inventory (Scarpelli et al., 2025).

Table S1. Methane flux datasets used to generate a prior emissions.

Sector	Source
Anthropogenic	EDGAR v8.0: Crippa et al. (2023)
Wetlands	NASA LPJ-EOSIM: (Colligan et al., 2024)
Fire	FINN: Wiedinmyer et al. (2023)
Geological	Etiope et al. (2019)
Termites	CAMS: Granier et al. (2019)
Rivers	Rocher-Ros et al. (2023)
Ocean	Weber et al. (2019)
Soil Sink	MeMo v1.0: Murguia-Flores et al. (2018)

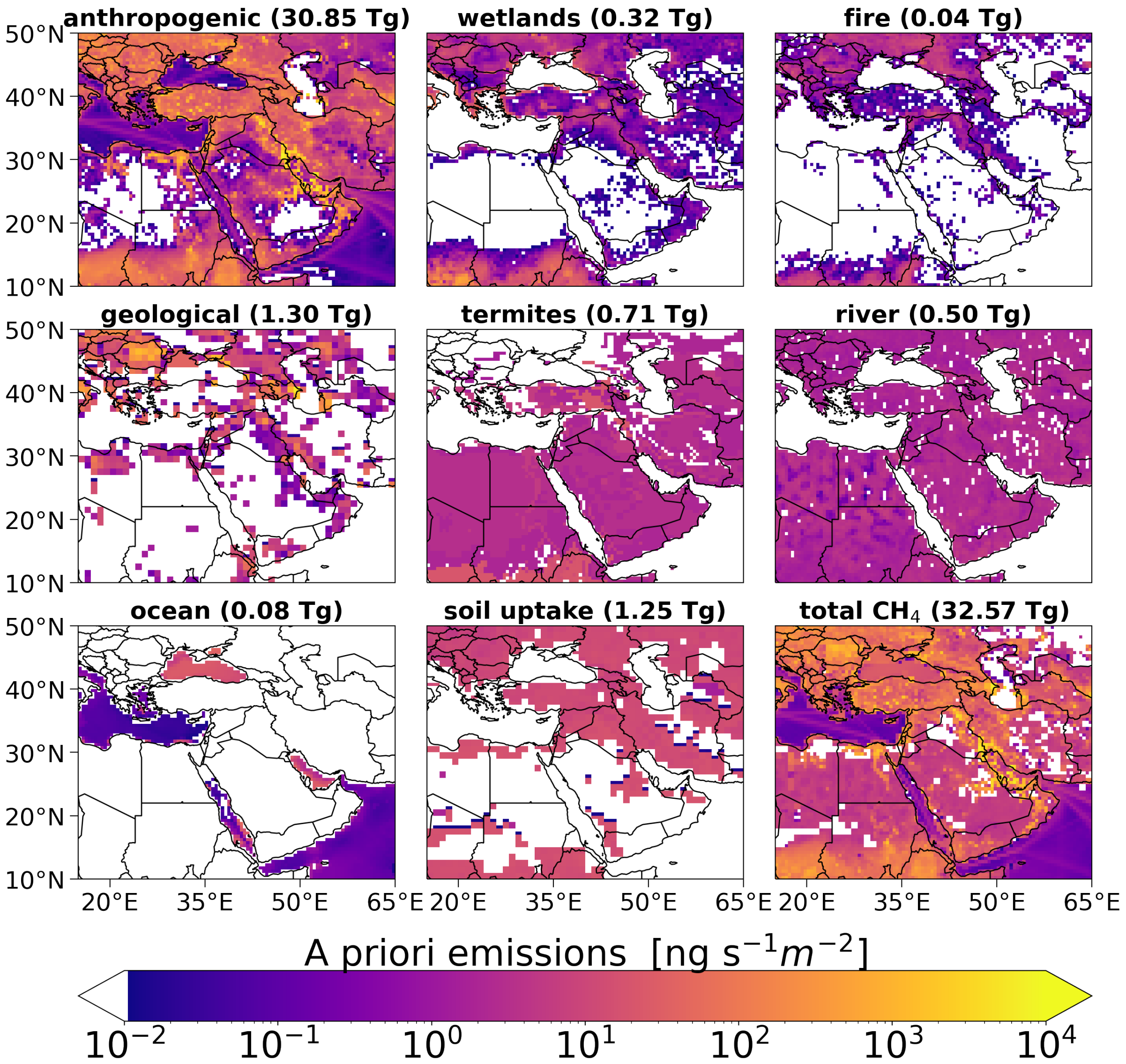

Figure S3. A priori methane emission source sectors including (1) anthropogenic emissions, (2) wetlands, (3) biomass burning, (4) geological sources, (5) termites, (6) rivers and streams, (7) shallow coastal waters and oceans, and (8) soil uptake (shown as positive values) fluxes. The lower right pannel shows the total CH_4 flux obtained from aggregating all sectors. Values in brackets indicate the total annual emissions for 2020 for each sector in the EMME region.

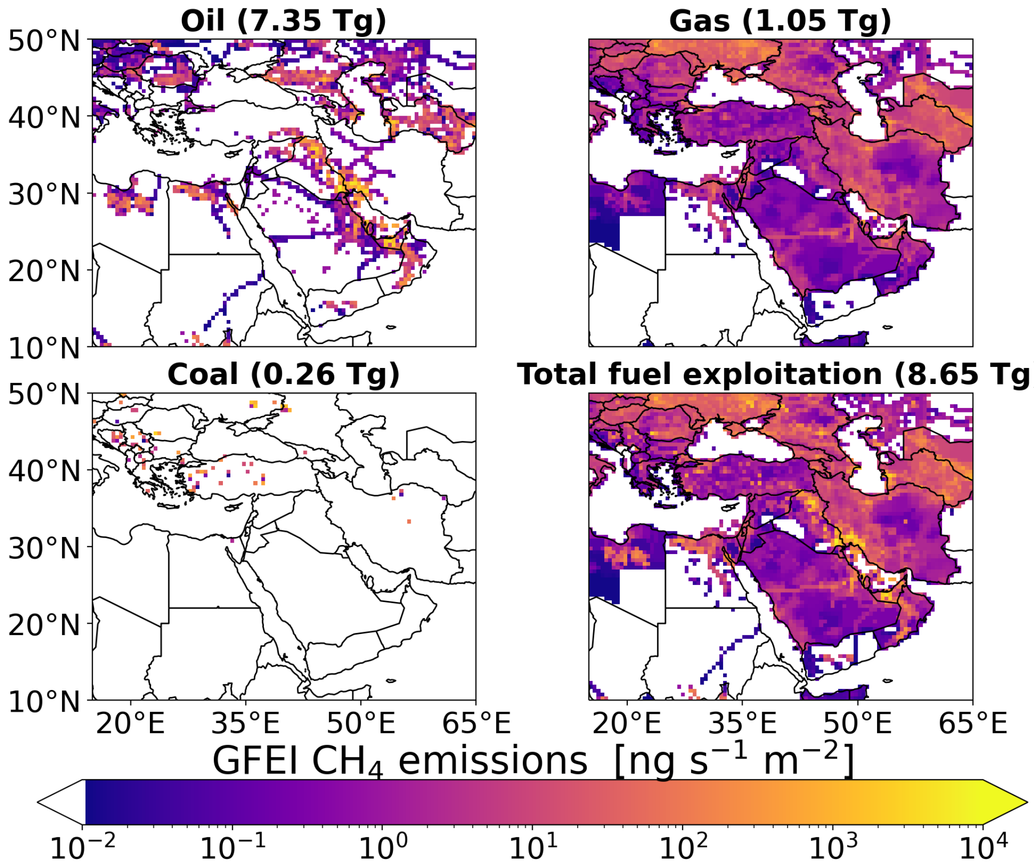

Figure S4. Methane emissions from fossil fuel exploitation for 2020 based on the GFEI v3 inventory: (i) oil, (ii) gas, (iii) coal, and (iv) total emissions from fossil fuel exploitation. Values in brackets indicate the total annual emissions for 2020 for each fuel exploitation sector in the EMME region. Note that total fuel exploitation emissions in the GFEI v3 inventory are substantially lower than in the EDGAR v8.0 inventory.

S3 Inversion grid

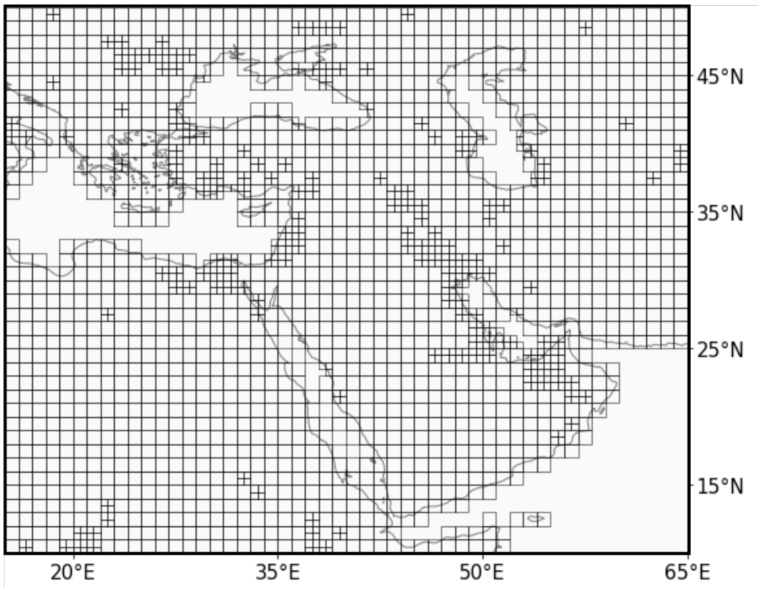

Figure S5. Inversion grid with variable grid sizes between 0.5°and 1.0°

S4 Validation

The scarcity of in situ measurements in the EMME region, which motivates the use of satellite observations for constraining the emissions, makes detailed validation against independent datasets challenging. Recently, however, the Total Carbon Column Observing Network (TCCON) was extended with a new station in Nicosia, Cyprus, as described by Rousogenous et al. (2026). TCCON is a global network of ground-based Fourier Transform Spectrometers that measure direct solar absorption spectra in the near-infrared. From these spectra, column-averaged mole fractions of the main greenhouse gases, are retrieved. The corresponding CH_4 dataset (Petri et al., 2024) is used here to validate our posterior results, providing an independent reference for assessing the accuracy of our satellite-based estimates.

Figure S6 shows our a priori and a posteriori modeled methane column mole fractions at the station, compared to the TCCON dataset. We observe an improvement in the agreement between the modeled values and the TCCON observations from the prior to the posterior estimates. The bias is reduced at the beginning and end of the time series and the seasonality is much better captured with the a posteriori values. Overall, the bias decreases from 11.1 ppb to 2.8 ppb, and the Pearson correlation increases from 7% to 66%.

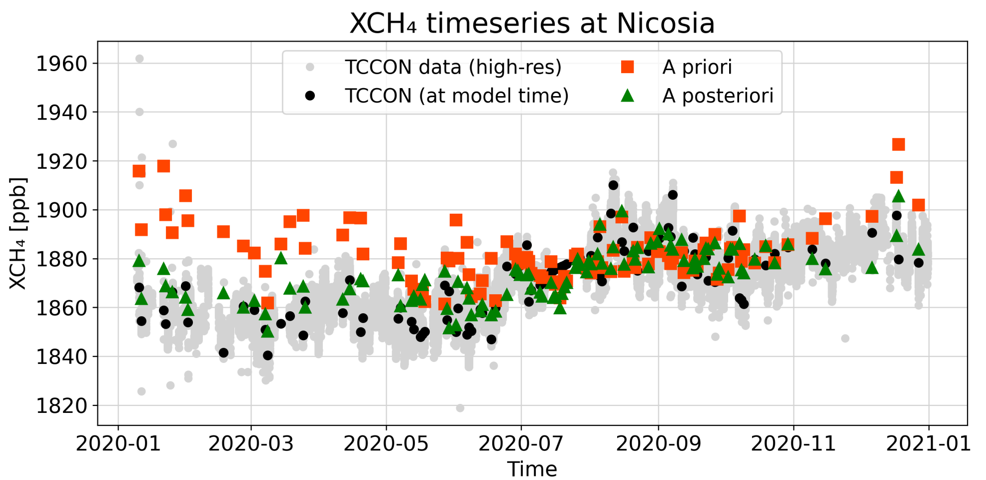

Figure S6. Methane time series of observed and modeled column mole fractions at the TCCON station in Nicosia. Red squares indicate the a priori modeled values, green triangles show the a posteriori values, while grey dots show the high-frequency TCCON observations and black dots the same observations interpolated to the model time steps.

S5 National emissions

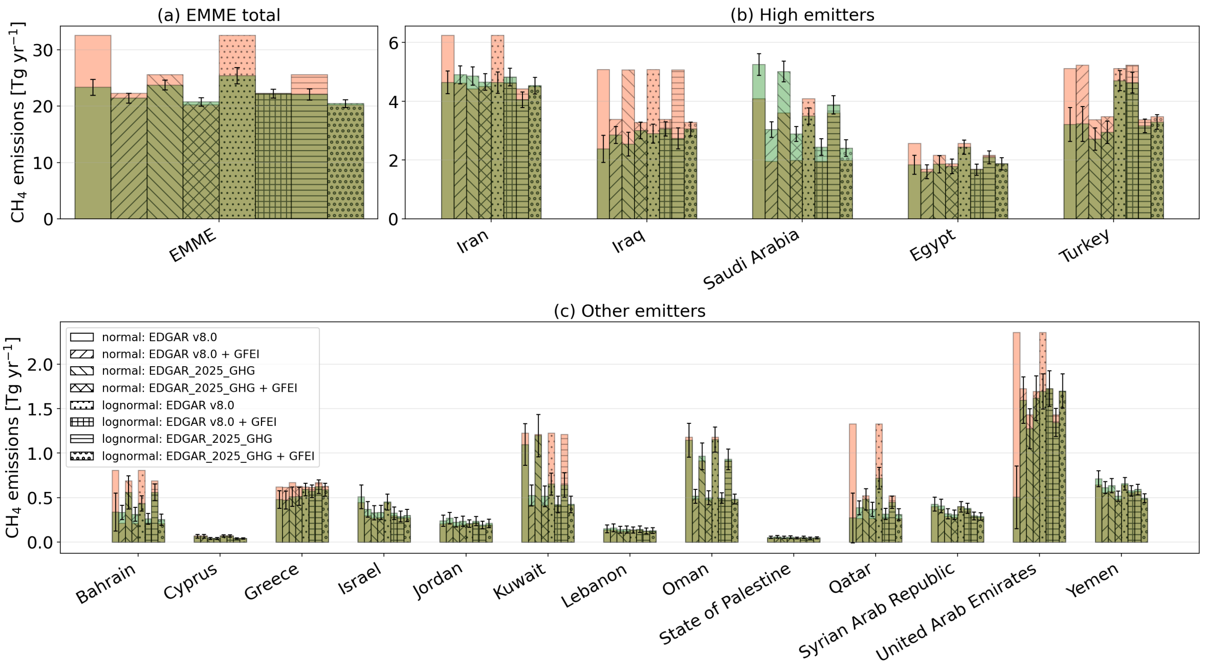

Figure S7. Inversion results for all the 8 cases, combining the four a priori inventories with the two error distribution choices. A priori (red) and a posteriori (green) values are shown using overlaid bars: red shading, therefore, indicates downward corrections, while light green shading indicates upward corrections relative to the a priori emissions. Error bars indicate the 1σ uncertainty derived from the respective Monte Carlo ensembles.

Table S2. Total 2020 CH_4 emissions for the EMME region and individual countries, shown with associated 1σ uncertainties.

Country	CH_4 posterior [Tg yr^{-1}]
Iran (Islamic Republic of)	4.642 ± 0.402
Saudi Arabia	3.558 ± 1.066
Turkey	3.492 ± 0.813
Iraq	2.822 ± 0.405
Egypt	1.899 ± 0.351
United Arab Emirates	1.433 ± 0.451
Oman	0.774 ± 0.308
Kuwait	0.686 ± 0.320
Yemen	0.600 ± 0.095
Greece	0.545 ± 0.103
Qatar	0.414 ± 0.185
Bahrain	0.383 ± 0.167
Israel	0.364 ± 0.112
Syrian Arab Republic	0.353 ± 0.079
Jordan	0.228 ± 0.058
Lebanon	0.141 ± 0.039
Cyprus	0.054 ± 0.020
State of Palestine	0.053 ± 0.014
EMME region	22.440 ± 1.854

Table S3. National emissions reported to the UNFCCC. For countries without a 2020 estimate, the closest available year is used for comparison with our inversion results. Greece is highlighted as the only Annex-I country in the EMME region, required to report annual emissions.

Country	Reported year	Source
Bahrain	2022	Kingdom of Bahrain (2024)
Cyprus	2020	Cyprus (2023)
Egypt	2020	Arab Republic of Egypt (2025)
Greece	**2020**	**Greece (2024)**
Iran	2010	Islamic Republic of Iran (2017)
Iraq	2019	Republic of Iraq (2024)
Israel	2020	Israel (2025)
Jordan	2020	Hashemite Kingdom of Jordan (2025)
Kuwait	2016	State of Kuwait (2019)
Lebanon	2019	Lebanon (2022)
Oman	2022	Sultanate of Oman (2025)
Qatar	2022	State of Qatar (2025)
Saudi Arabia	2019	Kingdom of Saudi Arabia (2024)
State of Palestine	2011	State of Palestine (2016)
Syrian Arab Republic	2005	Syrian Arab Republic (2010)
Turkey	2020	Türkiye (2023)
United Arab Emirates	2021	United Arab Emirates (2023)
Yemen	2012	Republic of Yemen (2017)

S6 Emission timeseries

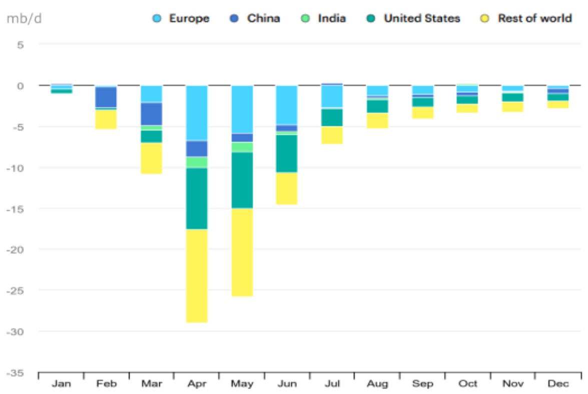

Figure S8. Oil demand in 2020 compared to 2019 (International Energy Agency, 2020).

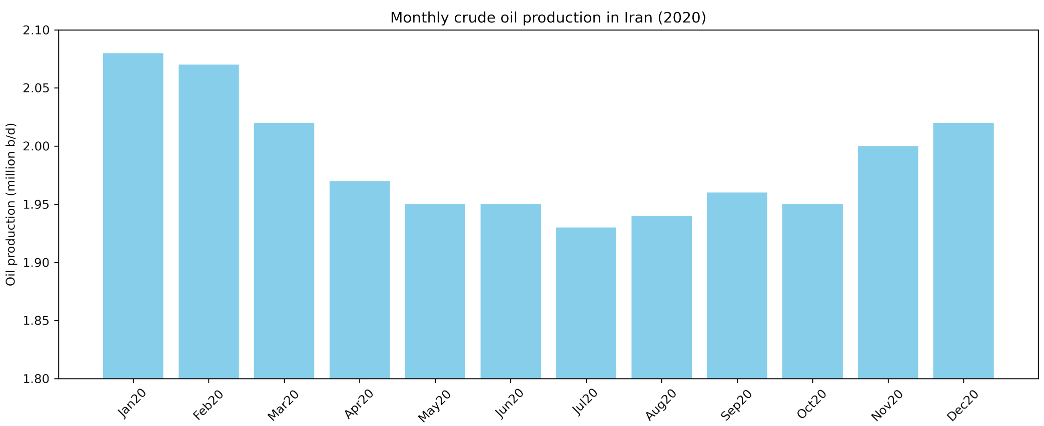

Figure S9. Monthly crude oil production (TradingEconomics.com, 2026)

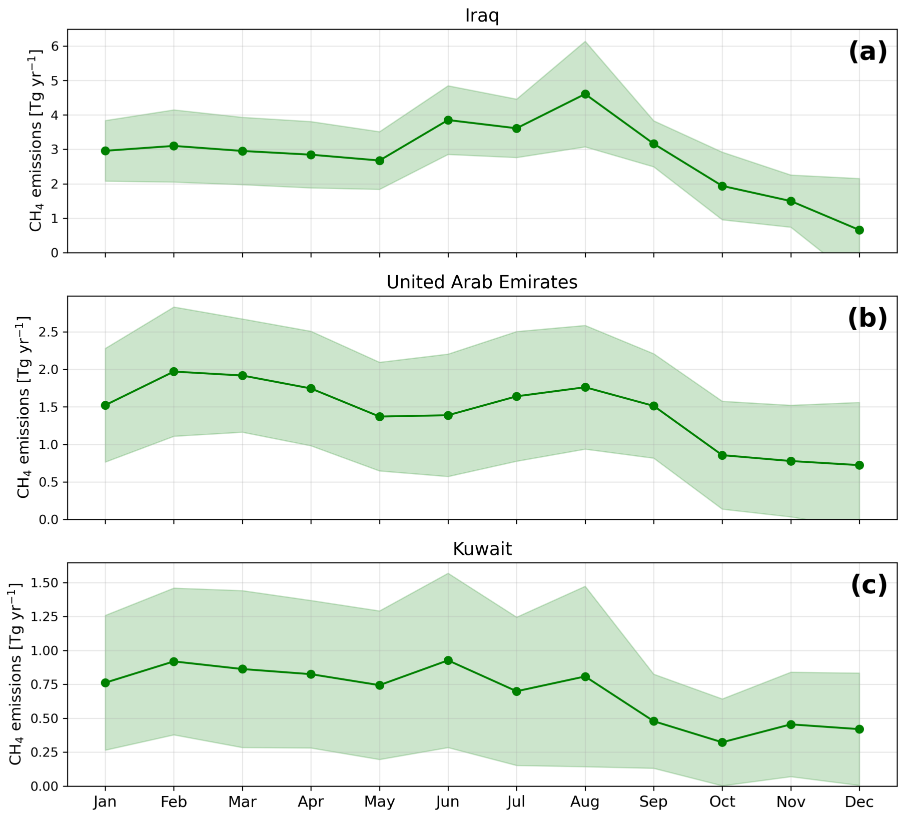

Figure S10. Time series of monthly a posteriori emissions over the year 2020 for (a) Iraq, (b) United Arab Emirates, and (c) Kuwait

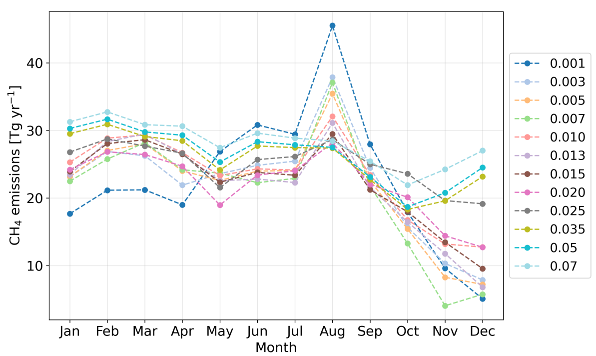

Figure S11. Time series of monthly total a posteriori emissions over the year 2020 for the EMME region for different assumed baseline uncertainties (dashed colored lines).

S7 Regression analysis

We perform a regression analysis to assess the extent to which posterior national methane emissions from the fuel exploitation sector scale with oil and gas production in the EMME region. To approximate fuel exploitation emissions from our inversion-derived total emissions, we use sectoral emission shares from the EDGAR_2025_GHG dataset. Data on domestic crude oil and natural gas production were compiled independently from IEA and are summarized in Table S4. We first apply a weighted least squares regression for the major producing countries:

$$\mathbf{E} = a + b_{\text{oil}}\mathbf{X}_{\text{oil}} + c_{\text{gas}}\mathbf{X}_{\text{gas}} \tag{1}$$

solving

$$\min \sum_i \mathbf{w}_i \left(\mathbf{E}_i - \hat{\mathbf{E}}_i\right)^2 \tag{2}$$

where $\mathbf{E}_i$ denotes the posterior emissions for country i, $\hat{\mathbf{E}}_i$ is the model emission estimate, $\mathbf{X}_{\text{oil},i}$ and $\mathbf{X}_{\text{gas},i}$ represent scaled oil and gas production, respectively, and $\mathbf{w}_i$ are reflecting the weights ($\boldsymbol{\sigma}_i^{-2}$) based on the emission uncertainties of each country-level emission estimate. The coefficients a, b_{oil}, and c_{gas} correspond to the intercept and the sensitivities of emissions to oil and gas production. This analysis is intended as a diagnostic tool rather than a predictive model, as it assumes a simplified linear relationship with constant emission factors across countries, similar to the approach used in some bottom-up inventories, thereby allowing us to assess the extent to which such uniform scaling can explain the observed variability. While the use of sectoral emission shares from prior inventories introduces additional uncertainty in the derived fuel-sector emissions, we assume the effect on the qualitative patterns and conclusions to be limited.

We derive the regression parameters of: a = 1.17, b_{oil} = 0.74, and c_{gas} = 0.21, indicating a higher sensitivity of emissions to oil than to gas production. However, the regression gives a poor fit with an R^2 value of 0.291 overall, while individual countries exhibit substantial deviations from the fitted relationship (Fig. S12).

In particular, Iran and Iraq show higher-than-expected emissions, whereas Saudi Arabia, Kuwait, and Qatar exhibit lower-than-expected values relative to the regression predictions. This pattern is broadly consistent with Chen et al. (2023), who report low methane intensities[1] for Saudi Arabia (0.14%), Kuwait (0.15%), and Qatar (0.06%) which have been attributed to modern infrastructure and effective associated gas capture. In contrast they reported highest methane intensity for Iraq (17.6%), interpreted as leaky infrastructure combined with venting or incomplete flaring, consistent with the positive residuals found in our analysis. Overall, these results indicate substantial cross-country heterogeneity in emission intensities, suggesting that factors beyond production (such as infrastructure, operational practices, and mitigation measures) play an important role.

In addition, we perform a regression including all countries in the EMME region[2], which increases the R^2 to 0.52 and yields coefficients of $a = 0.73$, $b_{\text{oil}} = 1.04$, and $c_{\text{gas}} = 0.21$. While absolute residuals are small for lower-producing countries,

[1] defined as upstream oil–gas emissions per unit of gas production

[2] except for Lebanon, Cyprus, and the State of Palestine, for which production data were not available

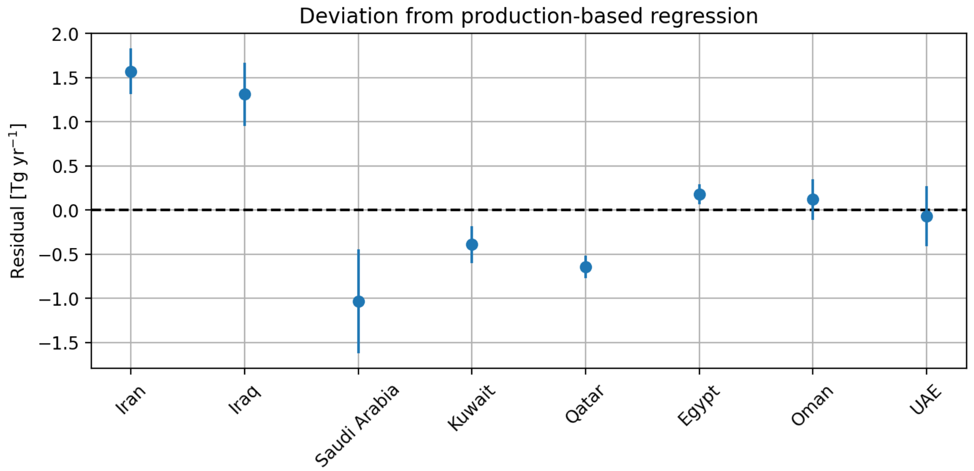

Figure S12. Deviations of national fuel-sector emissions from values predicted by the regression using oil and gas production data for major producing countries in the EMME region.

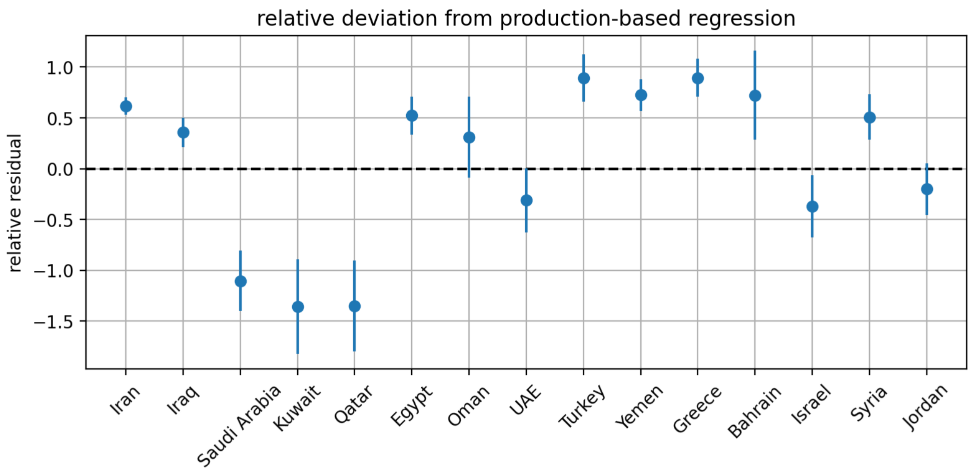

Figure S13. Relative deviation of national fuel-sector emissions from values predicted by the regression using oil and gas production data for countries in the EMME region.

their relative residuals are comparable in magnitude to those of major producers (Fig. S13, notice pronounced negative relative increments for Saudi Arabia, Kuwait, and Qatar). We attribute the increase in R^2 primarily to the expanded range of emissions when including lower-producing countries. The persistently large relative residuals across all countries indicate that the underlying fit quality does not substantially improve, further highlighting the importance of factors beyond production.

Table S4. Domestic crude oil production and domestic gas production data used in the regression analysis (International Energy Agency, n.d.). Countries are separated into high- and low-producing groups

Country	**Oil** [TJ]	**Gas** [TJ]
High-producing countries		
Egypt	1,329,858	2,156,909
Iran	5,084,082	9,103,366
Iraq	8,627,439	252,054
Kuwait	5,757,813	560,880
Oman	1,998,122	1,360,171
Qatar	2,968,905	6,212,732
Saudi Arabia	22,058,638	3,378,668
UAE	7,529,390	1,867,280
Low-producing countries		
Bahrain	445,839	567,203
Greece	3,874	279
Israel	5,548	528,103
Jordan	75	5,237
Syria	82,501	92,968
Turkey	137,085	15,212
Yemen	154,125	721

S8 Sensitivity tests

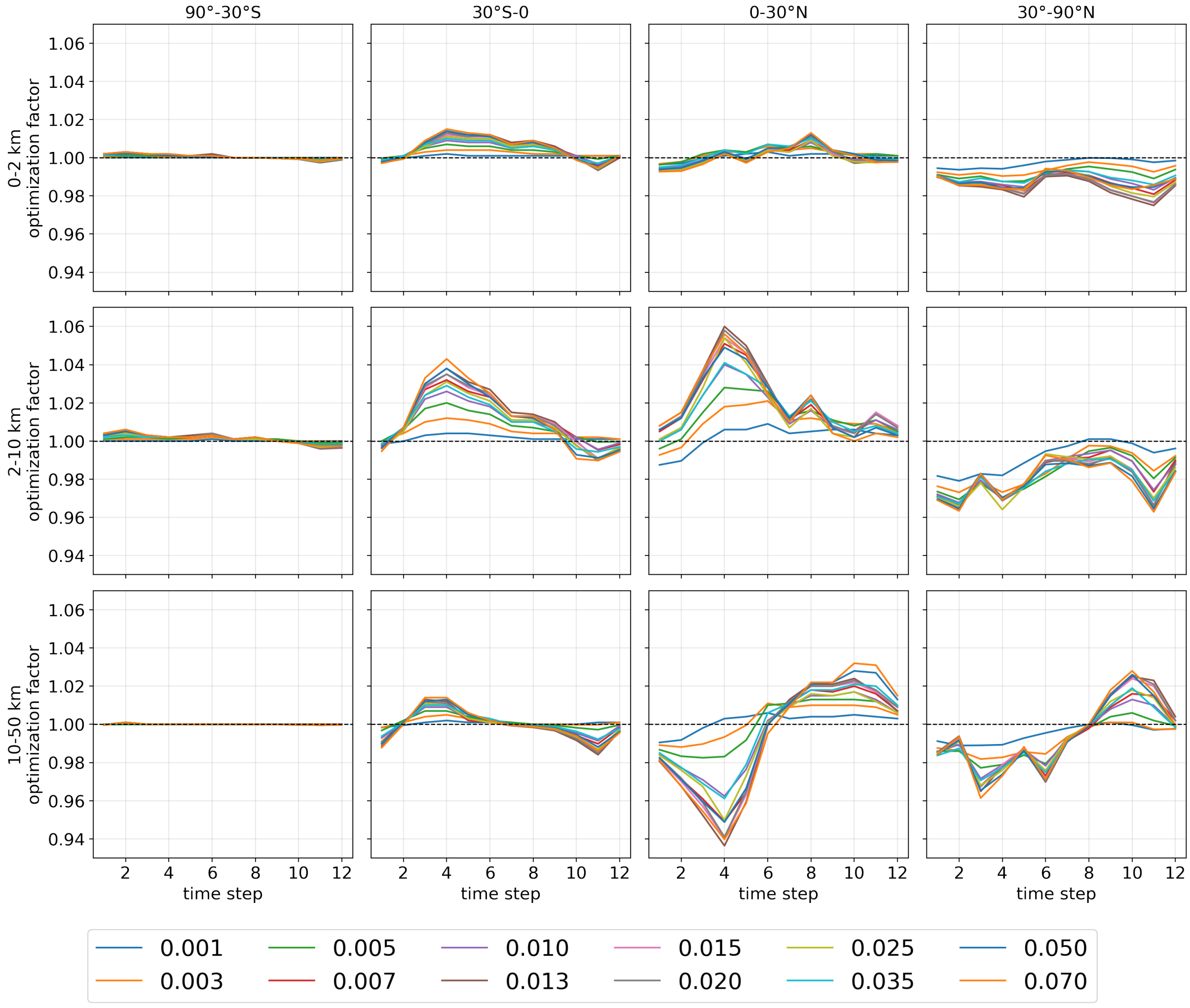

Figure S14. Optimized baseline factors are shown for multiple baseline uncertainties between 0.1% and 7% (colored lines).

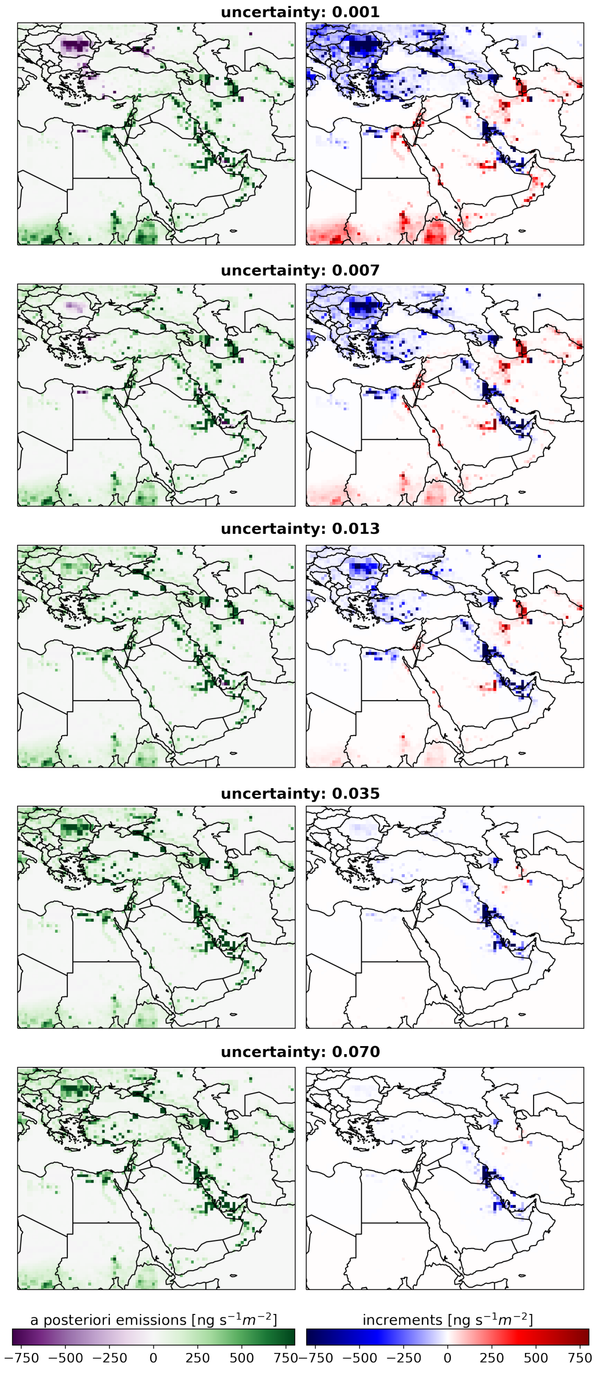

Figure S15. A posteriori emissions and inversion increments, shown for multiple baseline factor uncertainties between 0.1% and 7%.

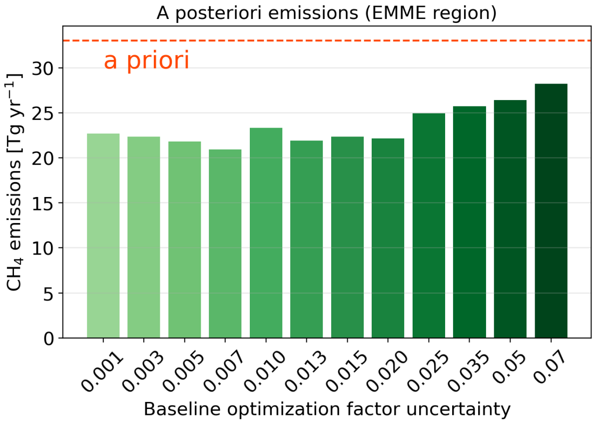

Figure S16. Total a posteriori emissions in the EMME region shown for multiple baseline factor uncertainties between 0.1% and 7%.

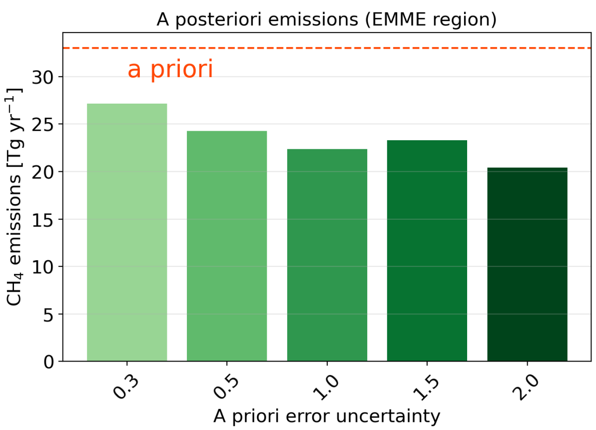

Figure S17. Total a posteriori emissions in the EMME region shown for multiple a priori emission uncertainties between 30% and 200%.

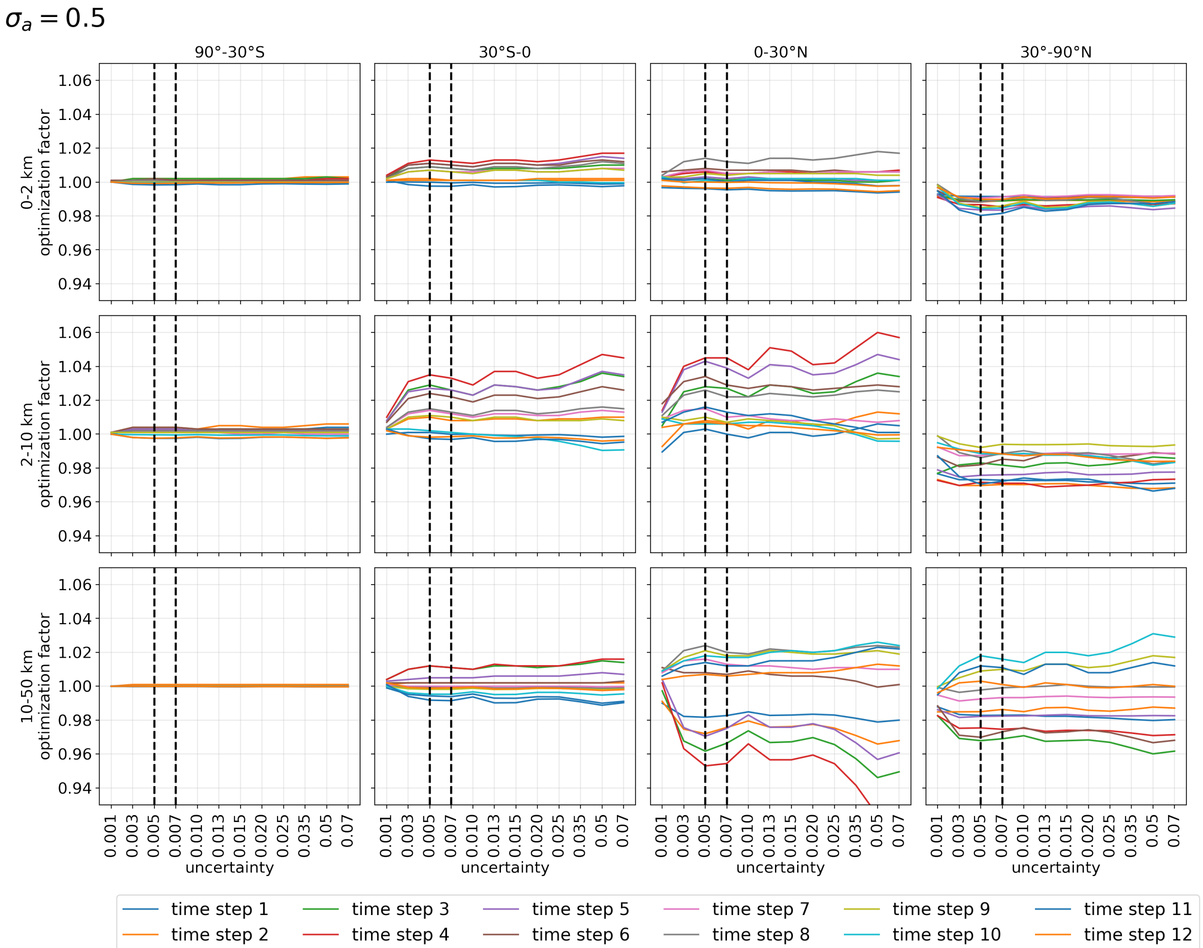

Figure S18. Optimized baseline factors for an a priori uncertainty of 50%, shown for all coarse grid cells and as a function of baseline uncertainties between 0.1% and 7%. The vertical dashed lines are interpreted as the transition zone between effective bias correction and the onset of compensation effects

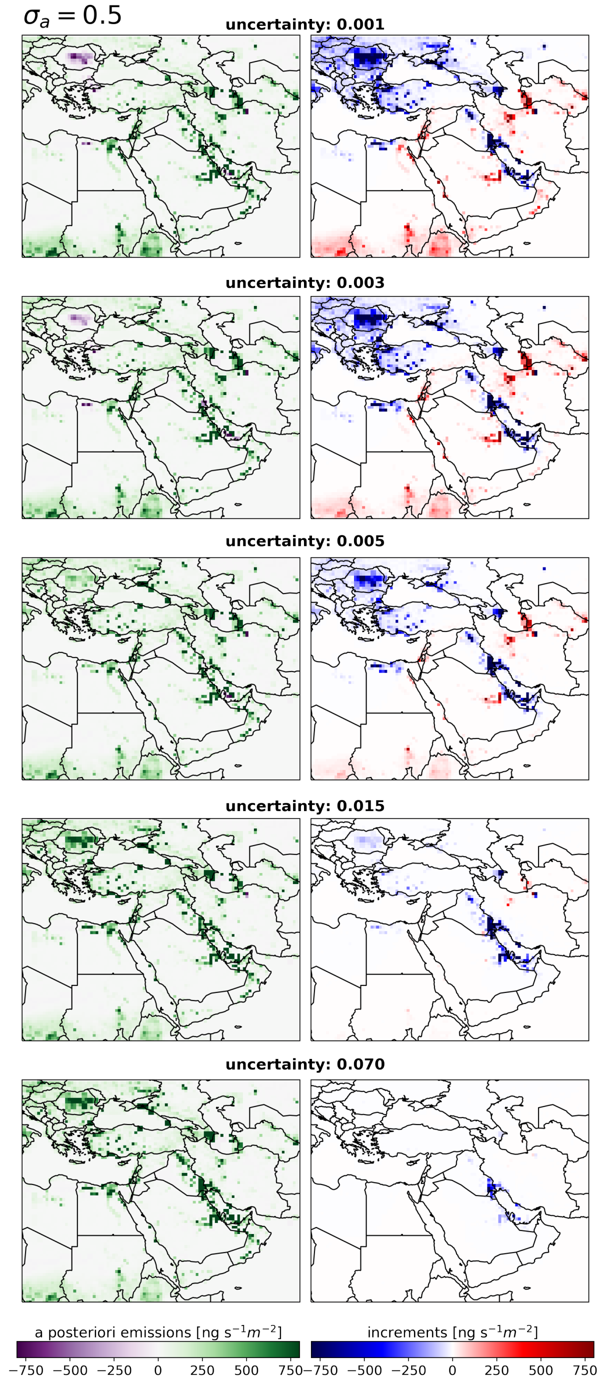

Figure S19. A posteriori emissions and inversion increments for an a priori uncertainty of 50%, shown for multiple baseline factor uncertainties between 0.1% and 7%.

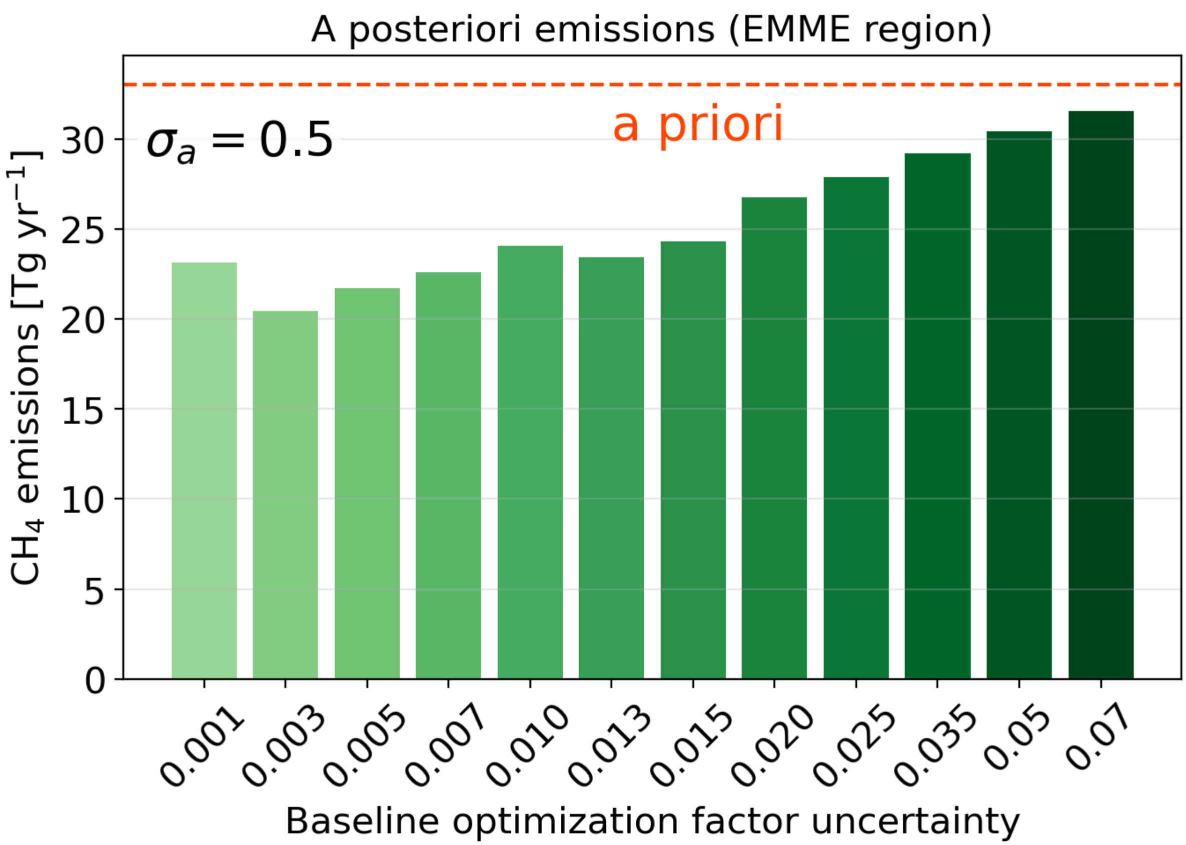

Figure S20. Total a posteriori emissions in the EMME region for an a priori uncertainty of 50%, shown for multiple baseline factor uncertainties between 0.1% and 7%.

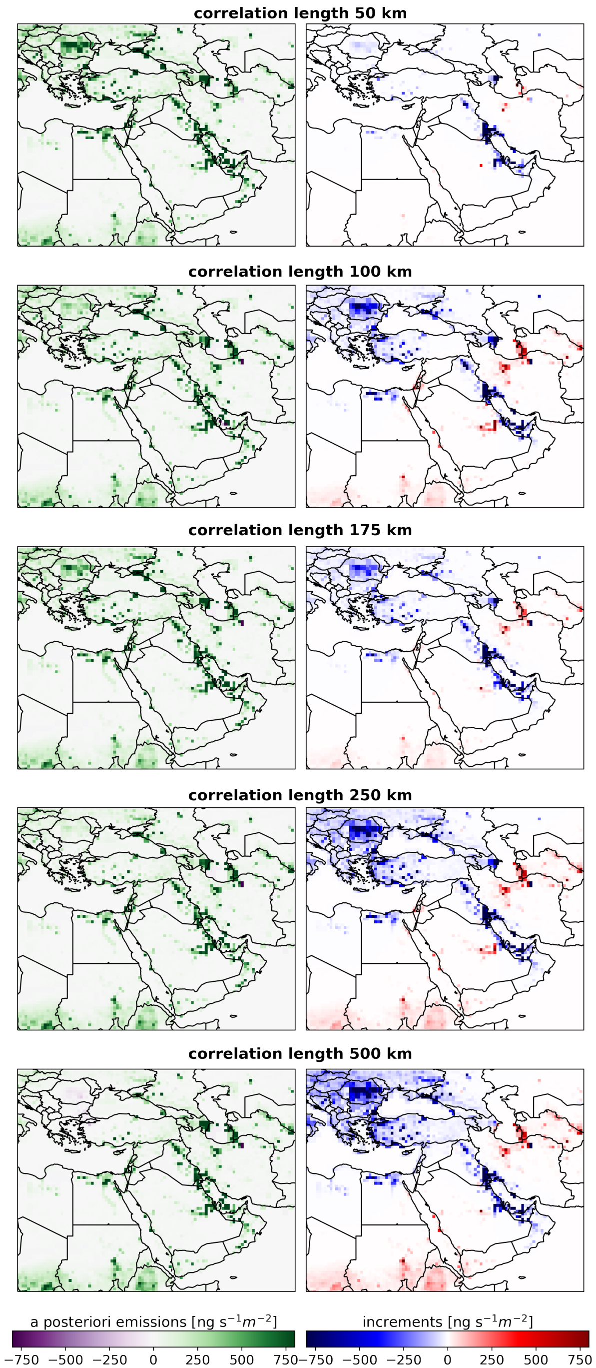

Figure S21. A posteriori emissions and inversion increments, shown for multiple a priori error correlations between 50 km and 500 km.

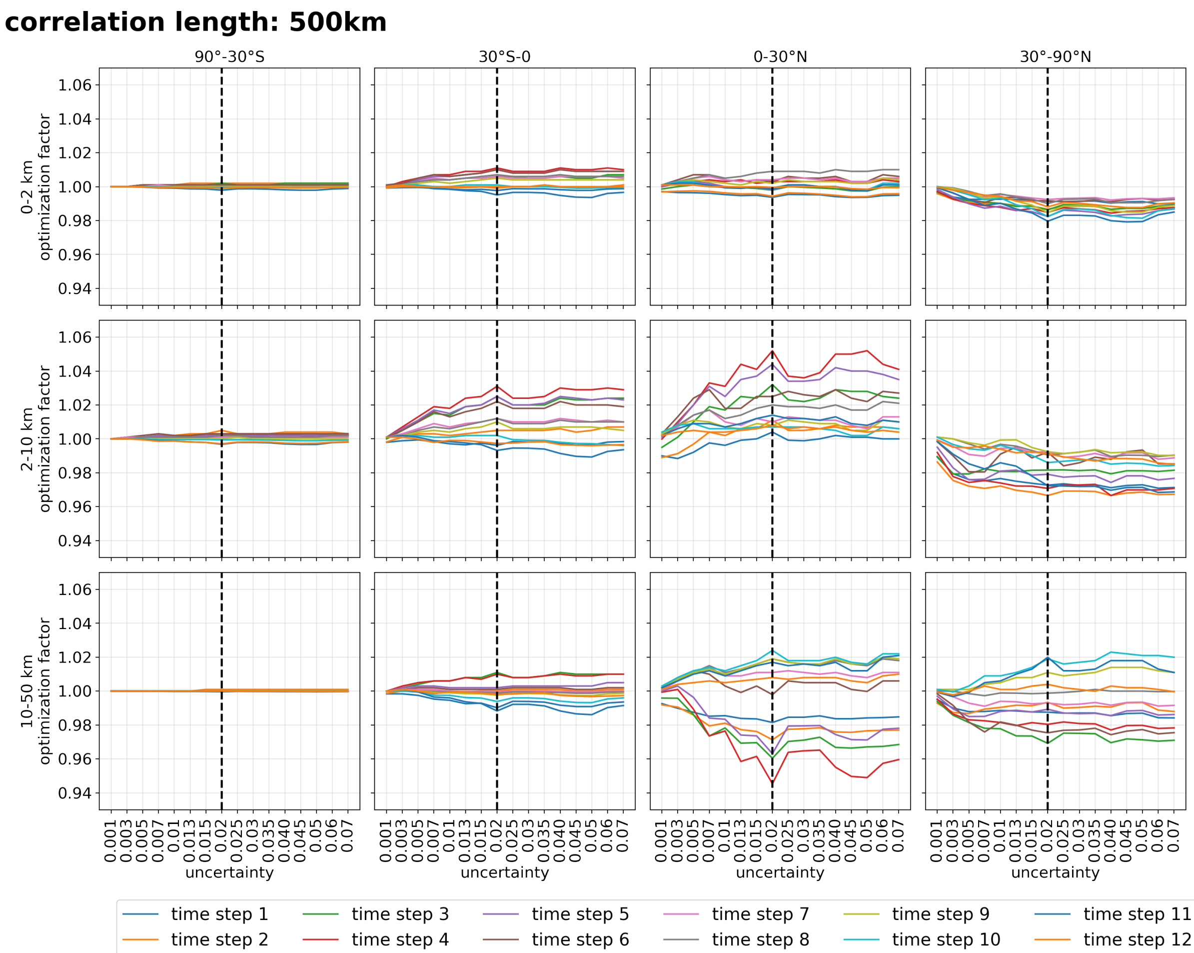

Figure S22. Optimized baseline factors for an a priori uncertainty correlation of 500 km, shown for all coarse grid cells and as a function of baseline uncertainties between 0.1% and 7%. The vertical dashed line is interpreted as the transition between effective bias correction and the onset of compensation effects

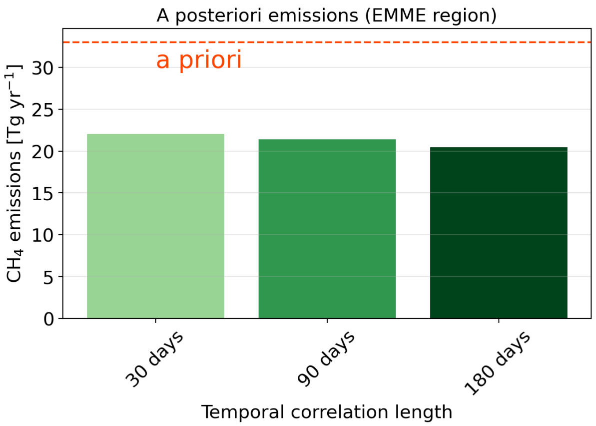

Figure S23. Total a posteriori emissions in the EMME region shown for temporal a priori emission uncertainty correlations of 30, 90 and 180 days.

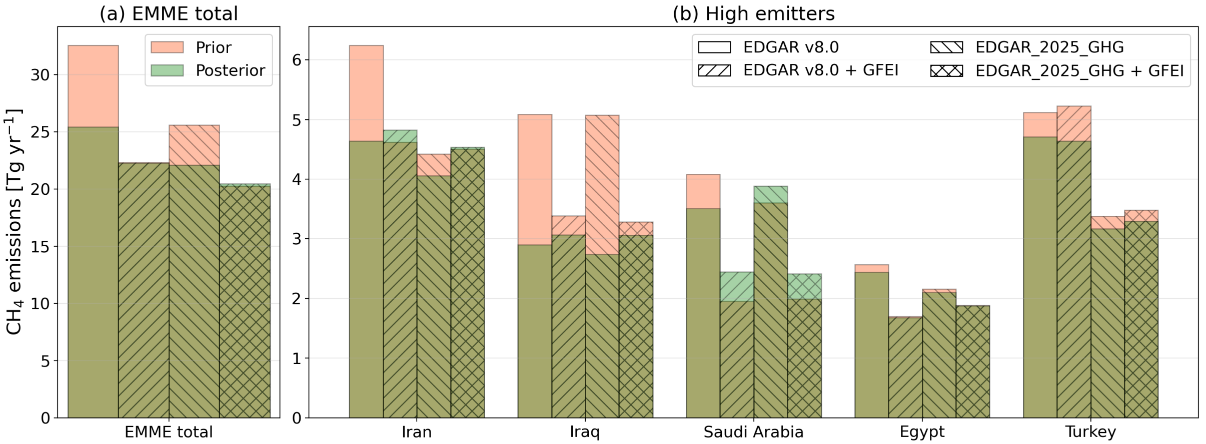

Figure S24. A priori and a posteriori emissions resulting from inversions with different prior inventories when using a lognormal a priori error distribution

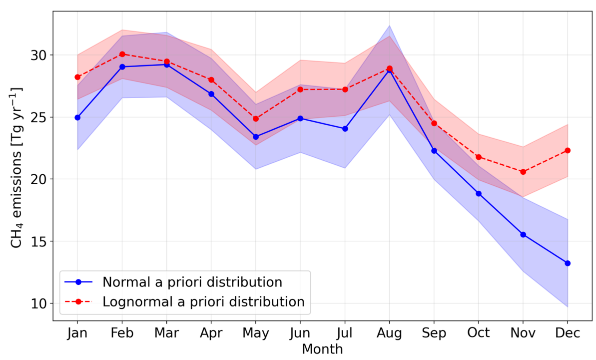

Figure S25. A posteriori emission timeseries when using a normal and a lognormal a priori error distribution.

References

Arab Republic of Egypt: First Biennial Transparency Report to the United Nations Framework Convention on Climate Change, https://unfccc.int/sites/default/files/resource/Egypt_BTR1_draft-%20Report_17September2025%20_TC_final.pdf, accessed: 2026-03-15, 2025.

Chen, Z., Jacob, D. J., Gautam, R., Omara, M., Stavins, R. N., Stowe, R. C., Nesser, H., Sulprizio, M. P., Lorente, A., Varon, D. J., et al.: Satellite quantification of methane emissions and oil–gas methane intensities from individual countries in the Middle East and North Africa: implications for climate action, Atmospheric Chemistry and Physics, 23, 5945–5967, https://doi.org/10.5194/acp-23-5945-2023, 2023.

Colligan, T., Poulter, B., and Quinn, C.: LPJ-EOSIM L2 Global Simulated Monthly Wetland Methane Flux V001, https://doi.org/10.5067/COMMUNITY/LPJ-EOSIM/LPJ_EOSIM_L2_MCH4E.001, accessed: 17 February 2026, 2024.

Crippa, M., Guizzardi, D., Pagani, F., Banja, M., Muntean, M., Schaaf, E., Becker, W., Monforti-Ferrario, F., Quadrelli, R., Risquez Martin, A., Taghavi-Moharamli, P., Köykkä, J., Grassi, G., Rossi, S., Brandao De Melo, J., Oom, D., Branco, A., San-Miguel, J., and Vignati, E.: GHG emissions of all world countries, Tech. Rep. JRC134504, Publications Office of the European Union, Luxembourg, https://doi.org/10.2760/953322, 2023.

Cyprus: Eighth National Communication and Fifth Biennial Report of Cyprus to the UNFCCC, https://unfccc.int/sites/default/files/resource/230607%20NC8_v2.1.pdf, accessed: 2025-04-09, 2023.

Etiope, G., Ciotoli, G., Schwietzke, S., and Schoell, M.: Gridded maps of geological methane emissions and their isotopic signature, Earth Syst. Sci. Data, 11, 1–22, https://doi.org/10.5194/essd-11-1-2019, 2019.

Granier, C., Darras, S., Denier van der Gon, H., Doubalova, J., Elguindi, N., Galle, B., Gauss, M., Guevara, M., Jalkanen, J.-P., Kuenen, J., Liousse, C., Quack, B., Simpson, D., and Sindelarova, K.: The Copernicus Atmosphere Monitoring Service global and regional emissions (April 2019 version), Report, Copernicus Atmosphere Monitoring Service (CAMS), https://doi.org/10.24380/d0bn-kx16, 2019.

Greece: National Inventory Report for Greenhouse Gas Emissions 1990–2022: Submission under the United Nations Framework Convention on Climate Change and the Kyoto Protocol, https://unfccc.int/documents/645148, accessed: 2024-04-09, 2024.

Hashemite Kingdom of Jordan: First Biennial Transparency Report to the United Nations Framework Convention on Climate Change, https://unfccc.int/sites/default/files/resource/Jordan%20First%20BTR_6Nov.pdf, accessed: 2026-03-15, 2025.

International Energy Agency: Change in Monthly Oil Demand in Selected Countries, 2020 Relative to 2019, https://www.iea.org/data-and-statistics/charts/change-in-monthly-oil-demand-in-selected-countries-2020-relative-to-2019, licence: CC BY 4.0, 2020.

International Energy Agency: Countries, https://www.iea.org/countries/, accessed: 2026-04-17, n.d.

Islamic Republic of Iran: Third National Communication to the United Nations Framework Convention on Climate Change (UNFCCC), https://unfccc.int/sites/default/files/resource/Third%20National%20communication%20IRAN.pdf, accessed: 2025-04-09, 2017.

Israel: First Biennial Transparency Report (BTR1) and Fourth National Communication (NC4) to the United Nations Framework Convention on Climate Change (UNFCCC), https://unfccc.int/sites/default/files/resource/Israel%27s%20first%20Biennial%20Transparency%20Report%20and%20fourth%20National%20Communication%20Report%202025%20%287%29%20%282%29_compressed.pdf, accessed: 2026-03-15, 2025.

Kingdom of Bahrain: First Biennial Transparency Report to the United Nations Framework Convention on Climate Change, https://unfccc.int/sites/default/files/resource/30112025_Bahrain%27s_BTR1_2024_to_the_UNFCCC_vSubmitted.pdf, accessed: 2026-03-15, 2024.

Kingdom of Saudi Arabia: Second Biennial Update Report to the United Nations Framework Convention on Climate Change, https://unfccc.int/sites/default/files/resource/Kingdom%20of%20Saudi%20Arabia%C2%A0Bur2.pdf, accessed: 2026-03-15, 2024.

Lebanon: Lebanon's Fourth National Communication (NC4) on Climate Change to the United Nations Framework Convention on Climate Change (UNFCCC), https://www.undp.org/lebanon/publications/lebanons-4th-national-communication-climate-change, accessed: 2025-04-11, 2022.

Murguia-Flores, F., Arndt, S., Ganesan, A. L., Murray-Tortarolo, G., and Hornibrook, E. R. C.: Soil Methanotrophy Model (MeMo v1.0): a process-based model to quantify global uptake of atmospheric methane by soil, Geoscientific Model Development, 11, 2009–2032, https://doi.org/10.5194/gmd-11-2009-2018, 2018.

Petri, C., Vrekoussis, M., Rousogenous, C., Warneke, T., Sciare, J., and Notholt, J.: TCCON data from Nicosia (CY), Release GGG2020.R1 (Version R1), CaltechDATA, Dataset, https://doi.org/10.14291/tccon.ggg2020.nicosia01.R1, 2024.

Republic of Iraq: Second National Communication and First Biennial Update Report to the United Nations Framework Convention on Climate Change, https://unfccc.int/sites/default/files/resource/IRAQ%20SNCBUR%20-ENGLISH.pdf, accessed: 2026-03-15, 2024.

Republic of Yemen: First Biennial Update Report to the United Nations Framework Convention on Climate Change, https://unfccc.int/sites/default/files/resource/Yemen_%20First_BUR_2018.pdf, accessed: 2026-03-15, 2017.

Rocher-Ros, G., Stanley, E. H., Loken, L. C., and et al.: Global methane emissions from rivers and streams, Nature, 621, 530–535, https://doi.org/10.1038/s41586-023-06344-6, 2023.

Rousogenous, C., Petri, C., Quéhé, P.-Y., Laemmel, T., Laughner, J. L., Desservettaz, M., Pikridas, M., Ramonet, M., Bourtsoukidis, E., Buschmann, M., Notholt, J., Warneke, T., Paris, J.-D., Sciare, J., and Vrekoussis, M.: Extension of the Total Carbon Column Observing Network (TCCON) over the Eastern Mediterranean and Middle East: the Nicosia site in Cyprus, Atmos. Meas. Tech., 19, 565–581, https://doi.org/10.5194/amt-19-565-2026, 2026.

Scarpelli, T. R., Roy, E., Jacob, D. J., Sulprizio, M. P., Tate, R. D., and Cusworth, D. H.: Using New Geospatial Data and 2020 Fossil Fuel Methane Emissions for the Global Fuel Exploitation Inventory (GFEI) V3, Earth System Science Data, 17, 7019–7033, https://doi.org/10.5194/essd-17-7019-2025, 2025.

State of Kuwait: First Biennial Update Report to the United Nations Framework Convention on Climate Change, https://epa.gov.kw/Portals/0/PDF/FisrtBiennialUpdateEN.pdf, accessed: 2026-03-15, 2019.

State of Palestine: State of Palestine First National Communication (NC1) to the United Nations Framework Convention on Climate Change (UNFCCC), https://unfccc.int/sites/default/files/resource/Initial%20National%20Communication%20Report_%20State%20of%20Palestine.pdf, accessed: 2025-04-11, 2016.

State of Qatar: Second National Communication to the United Nations Framework Convention on Climate Change, https://cdn.climatepolicyradar.org/navigator/QAT/2025/qatar-national-communication-nc2_b68a2c4a1eda879f513943da057177ef.pdf, accessed: 2026-03-15, 2025.

Sultanate of Oman: First Biennial Transparency Report to the United Nations Framework Convention on Climate Change, https://unfccc.int/sites/default/files/resource/First%20BTR%20Oman%20UNFCCC%20Final.pdf, accessed: 2026-03-15, 2025.

Syrian Arab Republic: Initial National Communication of the Syrian Arab Republic to the United Nations Framework Convention on Climate Change (UNFCCC), https://unfccc.int/sites/default/files/resource/Syria_Initial%20National%20Communication.pdf, accessed: 2025-04-11, 2010.

Thompson, R. L., Krishnankutty, N., Pisso, I., Schneider, P., Stebel, K., Sasakawa, M., Stohl, A., and Platt, S. M.: Efficient use of a Lagrangian particle dispersion model for atmospheric inversions using satellite observations of column mixing ratios, Atmospheric Chemistry and Physics, 25, 12 737–12 751, https://doi.org/10.5194/acp-25-12737-2025, 2025.

TradingEconomics.com: Iran crude oil production, https://tradingeconomics.com/iran/crude-oil-production, accessed: 2026-04-02, 2026.

Türkiye: Türkiye Eighth National Communication (NC8) and Fifth Biennial Report (BR5) to the United Nations Framework Convention on Climate Change (UNFCCC), https://unfccc.int/sites/default/files/resource/8NC-5BR%20T%C3%BCrkiye.pdf, accessed: 2025-04-11, 2023.

United Arab Emirates: Fifth National Communications Report to the United Nations Framework Convention on Climate Change, https://unfccc.int/sites/default/files/resource/ncr%20report%20%20.pdf, accessed: 2026-03-15, 2023.

Weber, T., Wiseman, N. A., and Kock, A.: Global ocean methane emissions dominated by shallow coastal waters, Nature Communications, 10, 4584, https://doi.org/10.1038/s41467-019-12541-7, 2019.

Wiedinmyer, C., Kimura, Y., McDonald-Buller, E. C., Emmons, L. K., Buchholz, R. R., Tang, W., Seto, K., Joseph, M. B., Barsanti, K. C., Carlton, A. G., and Yokelson, R.: The Fire Inventory from NCAR version 2.5: an updated global fire emissions model for climate and chemistry applications, Geosci. Model Dev., 16, 3873–3891, https://doi.org/10.5194/gmd-16-3873-2023, 2023.